NIMPOL: An imaging polarimeter for the mid-infrared.

Craig H. Smith[1] Toby J.T. Moore[1,2] David K. Aitken[1,3]
Takuya Fujiyoshi[1]

[1]School of Physics, University College, UNSW, Australian Defence Force Academy, Canberra, ACT, 2600, Australia.
c-smith@adfa.oz.au, t-fujiyoshi@adfa.oz.au

[2] *current address:* Astrophysics Group, School of Electrical Engineering, Electronics and Physics, Liverpool John Moores University, Byrom St, Liverpool L3 3AF, UK
tjtm@staru1.livjm.ac.uk

[3] *current address:* Division of Physical Sciences, University of Hertfordshire, College Lane, Hatfield, HERTS AL10 9AB, UK
D.Aitken@roe.ac.uk

Abstract

We have built an imaging polarimeter for use at mid-infrared wavelengths (*i.e.* N band or 8 – 13 μm). The detecting element is a 128 x 128 element Si:Ga Focal Plane Array, supplied by Amber Engineering, USA. The polarimeter itself provides diffraction limited images on a 4-m class telescope and has a field of view of about 32 arcseconds of sky with 0.25 arcsecond pixels. We describe the optical design, control electronics, observing modes and detector sensitivities. Also presented are some observational results to demonstrate the power of this new imaging polarimetric system.

Keywords: Instrumentation: infrared, polarimetry

1 Introduction

At mid-infrared wavelengths, information about magnetic fields can be obtained from polarimetric observations, particularly in regions like the Galactic Centre (e.g. Smith, Aitken & Roche, 1988: Aitken et al., 1991), Orion (e.g. Aitken, Smith & Roche, 1989: Gonatas et al., 1990) and other star forming regions (e.g. Aitken, Smith, Roche & Wright, 1990: Aitken, Wright, Smith & Roche, 1993). Magnetic fields are thought to play a significant dynamical role in the process of star formation, and mid-infrared polarimetry is one of the few techniques which can determine the magnetic field structure in these heavily obscured sources. From the birth of stars in the interstellar medium to active galactic nuclei, magnetic fields often produce dynamically important and sometimes dominating effects. From previous studies that we have undertaken it has been found that the polarization (and hence magnetic fields) structures are complex, varying on extremely small spatial scales, and yet are present in large scale structures.

The best way to study these structures is with an imaging polarimeter, combining sub-arcsecond imaging/polarimetry with a wide field. We have constructed such an instrument, using a focal plane array (FPA) detector. The instrument was successfully commissioned at the 3.9m

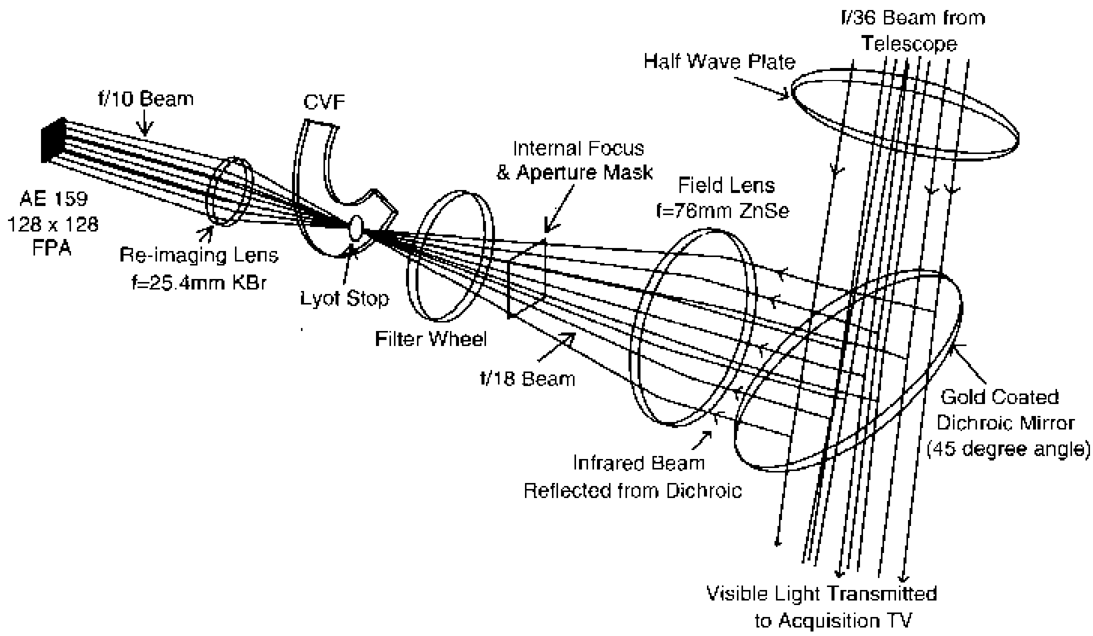

Figure 1: Schematic layout of NIMPOL optics.

Anglo-Australian Telescope (AAT) in July 1993. Of course, all instruments need an acronym and we have named our instrument NIMPOL (for N-band IMaging POLarimeter). This is the first and only mid-infrared imaging polarimeter in the world.

NIMPOL is the first stage of our instrumentation development program, and we are currently constructing a long-slit spectrometer (MIRAS for Mid-IR Array Spectro-polarimeter), utilising the same detector, readout and control system. Currently the planned commissioning date for the long-slit spectrometer is late 1996.

2 Optical Design

The optical design uses a simple and effective all refractive arrangement (see Figure 1) and all design goals were attained in actual operation at the telescope. An internal focus, (reimaged onto the detector), is required to allow masking of the image plane to accommodate a future polarization beam splitter.

For a 3.9-m telescope the diffraction disk at 10 μm represents about 0.54 arcseconds (FWHM) on the sky. The camera optics brings the focal ratio of the telescope from f/36 to f/10.8 on the detector which provides a diffraction spot size of $\sim 110\mu$m and a plate scale of 4.9 arcseconds/mm. The detector pixel size is 50μm square, giving 0.25 arcsecond pixels and a 32 arcsecond total field of view for the instrument. The diffraction disk (FWHM) is oversampled by the detectors at 10μm, and slightly undersampled at 8 μm.

A circular variable filter (CVF) and discrete filters are provided for wavelength selection. The CVF provides a spectral resolution of $\sim$ .25 μm over the 8 – 13 μm region, although its transmission efficiency is relatively low at $< 30\%$ average. The discrete filters have much better throughput (generally $>70\%$ for the broad band (BB) filters and $> 80\%$ for narrow band (NB) filters), and are used wherever possible. Table 1 provides a list of available filters. Although the detector/camera and readout electronics are capable of accepting broad-band photon fluxes, the narrow-band ($\Delta\lambda = 1\mu$m) filters are provided primarily to help separate emissive from absorptive

Name	Centre wavelength	Filter Width	Sensitivity
	μm	μm	mJy/arcsec^2/1 σ/1 min
10 μm BB	10.6	5.8	25
20 μm BB†	19.0	6.0	300
8.5 μm NB	8.5	1.0	46
11.5 μm NB	11.5	1.0	85
12.5 μm NB	12.5	1.0	100
SIV‡	10.52	0.1	210
NeII	12.81	0.1	310
CVF	8 – 14	.25	160 – 500

Table 1: Filters and sensitivities available in NIMPOL.
† The 20 μm BB filter can usually only be productively used at a dry site like Mauna Kea observatory, although it was used to observe η Carina at 17 μm from the AAT in 1994. Also the long wave cut off when observing with this filter is actually defined by the detector sensitivity which drops to zero at about 18 μm, so the effective wavelength coverage is 16 – 18 μm.
‡ Although the sensitivity in the SIV and NeII filters seems low, this figure really represents the sensitivity to continuum, and it is the narrowness of the filter which provides the sensitivity to the line emission, and separates it from continuum. The continuum can be determined using the CVF just off the line centre.

polarization, which have different polarization profiles over the 8 – 13 μm window. Two very narrow band filters are available for imaging in the forbidden transitions of SIV and NeII. At present we do not have special filters for imaging in the 8.6 and 11.25 μm unidentified infrared (UIR) features, but these filters can be obtained at moderate cost if required. The FPA currently in use has a Si:Ga detector layer which is sensitive from about 5 – 18 μm so use of the 20 μm filter in fact defines a passband about 2 μm wide centered on 17μm. However, detector efficiency is falling from 17 – 18 μm.

All components of the optics and the inside of the 4 K radiation shield were shot blasted, chemically etched and then matt black anodized to contain scattered light. All optical component mounts are aluminium to minimize the effects of differential contraction, except for the gears in drive trains, which were steel to avoid the binding effects of aluminium gears at cryogenic temperatures. The filter and CVF wheels are driven by warm stepping motors mounted on the outside if the dewar. The drive shafts were made from Vespel, for its low thermal conductivity properties. The rotary vacuum feedthroughs are Ferrofluidic seals. Each drive mechanism included a unique detent position and micro-switch for position sensing. The cryostat is an IR Labs HD-10 liquid helium and nitrogen cooled dewar, with a 2 litre helium capacity. This provides about 12-14 hours hold time without the detector running and about 10 hours hold time when the detector is running and at its optimum 18 – 20 K temperature. The detector is raised from the 4 K liquid helium temperature to 18 K by a small resistive heater mounted into the detector cold finger, and temperature controlled with a Lakeshore digital temperature controller. This controller is effective at keeping the detector temperature stable to less than 0.1° C. To minimize the extra heat required to keep the detector at its operational temperature, (thereby maximizing hold time) the detector mount block is thermally isolated by a teflon pad from the dewar cold plate. By selecting just the right thickness of teflon it is possible to make the cold block self-heat to about 16 K with heat generated by the detector itself, and a the resistive heater raises the block temperature just a few degrees to provide thermal stability with a minimum input of heat. The outside of the helium radiation shield is multi-layer wrapped with aluminized mylar.

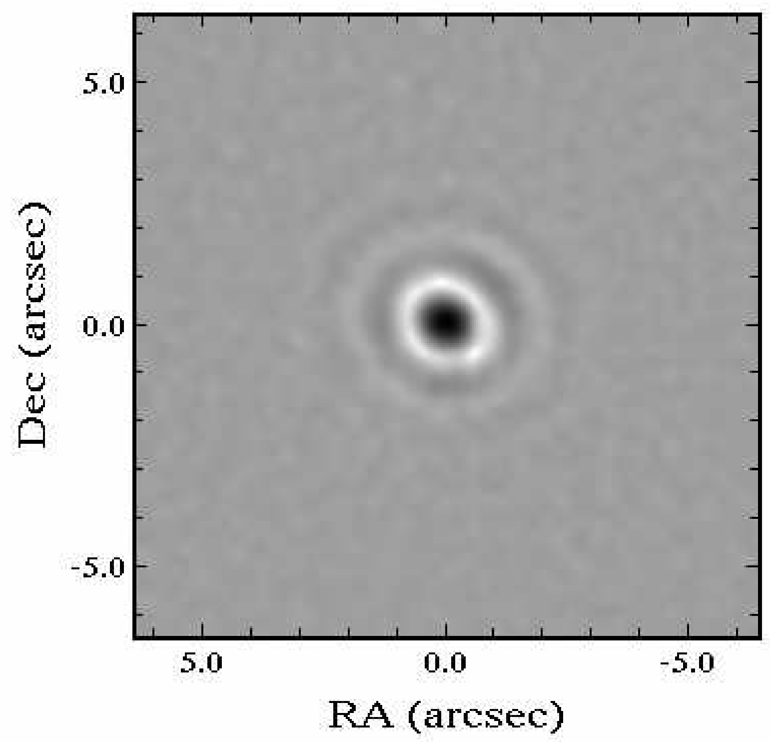

Figure 2: Image of γ Cru at 12.5 μm taken at the AAT in May 94. The first and second Airy maxima are seen clearly. This is a negative image, the dark central spot being the central maximum and the bright ring the first minimum.

The real imaging performance of the optical system can be seen in Figure 2 which shows an image of γ Crucis (taken from a subset of the array) showing clearly diffraction limited conditions at 12.5 μm. This image was taken at the AAT in May 1994, and is a coaddition of 32 frames each containing 800 ms integration. Registration of images is possible in real time, but in this case was unnecessary. In this image we clearly see the first two Airy maxima and a hint of the third. The first minimum is seen at 1.55 arcseconds diameter compared with $2.12\lambda/D = 1.40$ arcseconds calculated for a 3.9-m telescope with a 1.45 m central obstruction as at the AAT. The first Airy ring is enhanced because of the large central obstruction of the AAT primary and we find as much as 10% of the light in the rings. There is a very slight NE-SW elongation to the image which we attribute to the asymmetry of the chopping secondary. A $\lambda^{-1/5}$ wavelength dependence of seeing is expected and our infrared image is indeed half of the visible seeing disk measured to be 1.6 arcseconds (FWHM).

Our experience with the imaging system at the AAT after 3 years of operation there has been that when conditions are workable at all they are often (> 80 %) diffraction limited for 10 μm work.

In November 1995 we took NIMPOL to the ANU 2.3-m telescope, where the instrument operated successfully, except that, due to instabilities in the chopping secondary, the image quality was not optimal, and somewhat worse than the 1.2 arcsecond diffraction limit at 10 μm for this telescope. The main result of this inferior image quality, besides resolution, is a significant reduction in sensitivity to point or compact sources. Since this observing run however, the chopping secondary has been decommissioned and replaced with a tip-tilt system. The new secondary does not allow for chopping, which more or less precludes further observations with NIMPOL at the ANU 2.3m

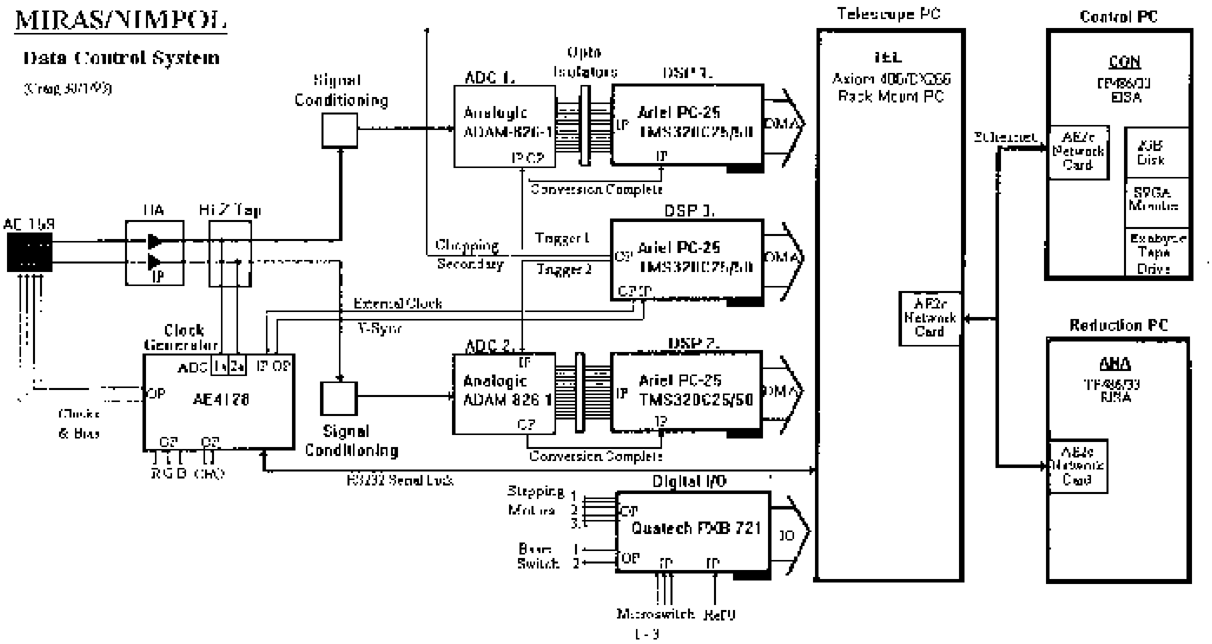

Figure 3: A schematic of the control and readout circuitry.

Well capacity	$\sim 2 \times 10^7$ electrons
Dark Current	$\sim$ 6000 electrons/s
Read Noise	$\sim$ 250 electrons
Quantum Efficiency	$\sim$ 7%
Photconductive Gain	$\sim$ 0.1
Detectivity, D*	$\sim 2 \times 10^{12}$ $\sqrt{\text{Hz}}$ cm/W
NEP	$< 1.5 \times 10^{-15}$ W/$\sqrt{\text{Hz}}$

Table 2: Detector Characteristics.

telescope, unless an operable STARE mode is developed. However, given the variable nature of the mid-infrared sky at Siding Spring Observatory we feel that operation (at these wavelengths) at this observatory site without a chopping secondary will never be entirely satisfactory.

3 Control and Data System

The Amber Engineering (AE 159) focal plane array has 128 $\times$ 128 detector elements, each 50 μm square on a Si-CMOS multiplexer. The detector material is Si:Ga, providing sensitivity from around 5 μm to $\sim$ 18 μm in wavelength. Other detector characteristics are provided in Table 2.

Some of the best features of this detector are its very deep wells, which coupled with fast readout electronics, make broadband imaging at the AAT possible, its very good uniformity, and operability (only four dead pixels in 16384). The sensitivity achieved to date, at the AAT is 100 mJy/arcsec^2/1 σ/1 min, λ = 12.5μm, $\Delta\lambda$=1μm. This however, is an on source sensitivity, and when chopping off chip is used this is a factor of 2.1 longer for actual elapsed time. Sensitivities obtained in the various filters at the AAT are included in Table 1. The quoted sensitivities were obtained at the AAT, with a sky temperature of about 5° C and 60 – 70 % relative humidity, in straight imaging mode. In polarimetry mode the sensitivity is reduced by a factor of about $\sqrt{3}$

by the inclusion of the wire grid analyser ($< 50\%$ transmission), and the warm waveplate which is a few per cent emissive. Sensitivities better by a factor of two or more would be expected when observing from a high altitude, cold, dry site like Mauna Kea observatory in Hawaii.

The detector has two analog outputs, which are fed through trans-impedance amplifiers and some other signal conditioning to two Analogic ADAM-846-1, 400 kHz, 16 bit, sample-and-hold, A/D converters. Sixteen bit A/D converters are required so that the noise can be adequately sampled by the A/D without the requirement for different gain or offset readings. The shot noise from a full well of 2×10^7 photo-electrons is 4472 electrons, and a 16 bit A/D which covers the full dynamic range of the detector has 305 photo-electrons per A/D unit. A/D converters with fewer bits would cause excessive digitization of the noise, particularly in low background situations where the detector well may be less than half full.

The nominal Sample-and-Hold plus A/D conversion time for the ADAM-846-1 is 2.4 μs per conversion, but we are running them nearer to 2 μs per conversion with no discernible loss in performance. Even so, the readout rate for the data system is still A/D conversion time limited. The two channels are readout simultaneously, so the minimum readout time for the array is 1.92 μs per pixel and 17.7 ms per array, which corresponds to a frame rate of 56 frames/s. This read rate, coupled with the deep wells (2×10^7 electrons) of the AE159 means that the readout electronics can handle detected photon rates of up to 1.1×10^9 ph/s.

The digitized data is then co-added on two 50 MHz Digital Signal Processors (Ariel Corp PC-25+ boards using a Texas Instruments TMS320C25/50 DSP chip). The analogue and digital electronics are separated by opto-isolators. A third DSP board generates the necessary clocking signals to operate the FPA and initiate A/D data conversion, as well as controlling the chop frequency of the oscillating secondary.

As well as cyclic clocking, the Amber AE159 chip has the ability to change its readout frequency from DC to 200 frames/s in real time, which means that it is not necessary to continue clocking and reading out the array when no useful function is performed. We operate the detector in this way to minimize non-productive time spent by the detector. The chip is always read out at the maximum possible rate for the data system (17.6 ms full frame), and longer integrations are obtained by suspending the clock for the required integration period, and then resuming clocking to readout the array. Integration times are increased from the minimum of 17.6 ms in one millisecond increments. This clocking method has no particular benefit in a STARE mode but when chopping is required we lose the minimum possible time waiting for the chop to settle. In this case the array is read out after an arbitrary length integration, clocking is then suspended, and the chop signal is generated. After the required amount of time for the chop to settle (5 – 10 ms) at the AAT, the array is clocked out, again at maximum speed, to flush unwanted integration while the secondary was moving, and then the real data integration is re-started. This means we only need to lose around 25 ms at each chop, even though the integration time may be much longer. This readout scheme is not required for broad band imaging at the fastest frame rates, but when narrow band filters are used, particularly the SIV and NeII filters, integrations become a significant fraction of a second to ensure the wells are reasonably filled and noise is dominated by photon noise rather than readout noise. Using this readout scheme does not seem to incur any penalty in extra readout noise from the array.

The DSPs are housed in a computer mounted at the telescope, and as the DSPs perform all of the time critical functions, we are able to use a relatively modest 486DX2-66MHz PC as the data acquisition control computer mounted at the telescope. The digital signal processor boards are the heart of the data acquisition system, and as throughput is generally a premium in mid-infrared instrumentation all of the time critical acquisition software was written in assembler and is uploaded to the DSP's from the control computer at the telescope. The DSP software also provides co-adding and co-subtracting of data and chop frames. The control software is designed to be as flexible as possible to allow for many different observing modes. The DSPs can change integration times, and also the number of coadded integrations per chop cycle and and number of coadded chop cycles before downloading to the control computer. In this way we optimize observing efficiency depending on conditions. In broad-band imaging we use short integrations, but with a number of coadds per chop cycle to keep the chop at what seems to be an optimal rate of a few Hz. Chopping faster than this reduces observing/integrating efficiency, but chopping slower provides increased noise.

The data is periodically downloaded to the host PC through direct memory access and then sent via an ethernet link to the main control computer where the data is processed, displayed and stored to disk. This communication and processing all occurs while the DSPs and the detector are coadding and integrating again, and so causes no efficiency loss.

Although there has been considerable discussion as to the necessity of chopping with array detectors in the thermal infrared, most evidence to date indicates that chopping at frequencies less than 1 Hz does incur an increased noise penalty. We have maintained an observing strategy of slow chopping and beamswitching to minimize the effects of sky background variations. However, we are still experimenting with other STARE type observing strategies. Given the necessity to chop, observing can only ever be 50% efficient on source, although on compact objects (*i.e.* a few arcseconds extension) and small chop/beamswitch throws ($<$ 15 arcseconds) it is possible to chop and beamswitch "on chip" to avoid the 50% loss in efficiency. Chop and beamswitch on chip (which produces four images, two positive and two negative) also reduces the chance for misregistration of the beam switch images. Otherwise great care is required when setting up the beam switch to ensure both positive and negative images fall on the same place on the detector. Whatever the case, our readout system is 97% efficient in spending time actually integrating (whether on sky or source) in imaging mode, and about 85% efficient in polarimetric mode where there are other overheads involved with waveplate rotation etc.

A third PC, also networked to the others by ethernet, provides off-line, but very nearly real time, reduction of the incoming data. By the end of the observation on an object, data coadding is complete, including shift and add if required. Flat fielding and flux calibration are applied in post-reduction. Both of these reductions could be included in real time reduction, but to date, we have found that calibrations have tended not to be firm until the end of the run and flat fielding is often unnecessary. The uniformity of the Amber array is such that images which are produced from chopped data are usually already flat and further flat-fielding only adds more noise. An exception to this was the 20 μm images where significant pixel-to-pixel non-uniformities were found and flat-fielding was required. In polarimetry mode though the external waveplate produces some vignetting of the field and more care with flat fielding is required here.

All of the control and reduction software was written in "C" . For image plotting routines it was found that normal "C" graphics routines were far too slow, so routines which directly address the PC graphics adapter memory were developed.

4 Polarimetry

Polarization measurements are made using a half wave plate to rotate the plane of polarization and a wire grid analyser (grid with 0.4 μm spacing on a KRS5 substrate). A CdS waveplate is used for 8 – 13 μm observations, and a CdSe waveplate is used at 20 μm. The waveplate is mounted outside the cryostat above the dichroic mirror, and is is rotated to four positions in the beam (corresponding to position angle rotations of 45°) and an intensity measurement I_θ is made

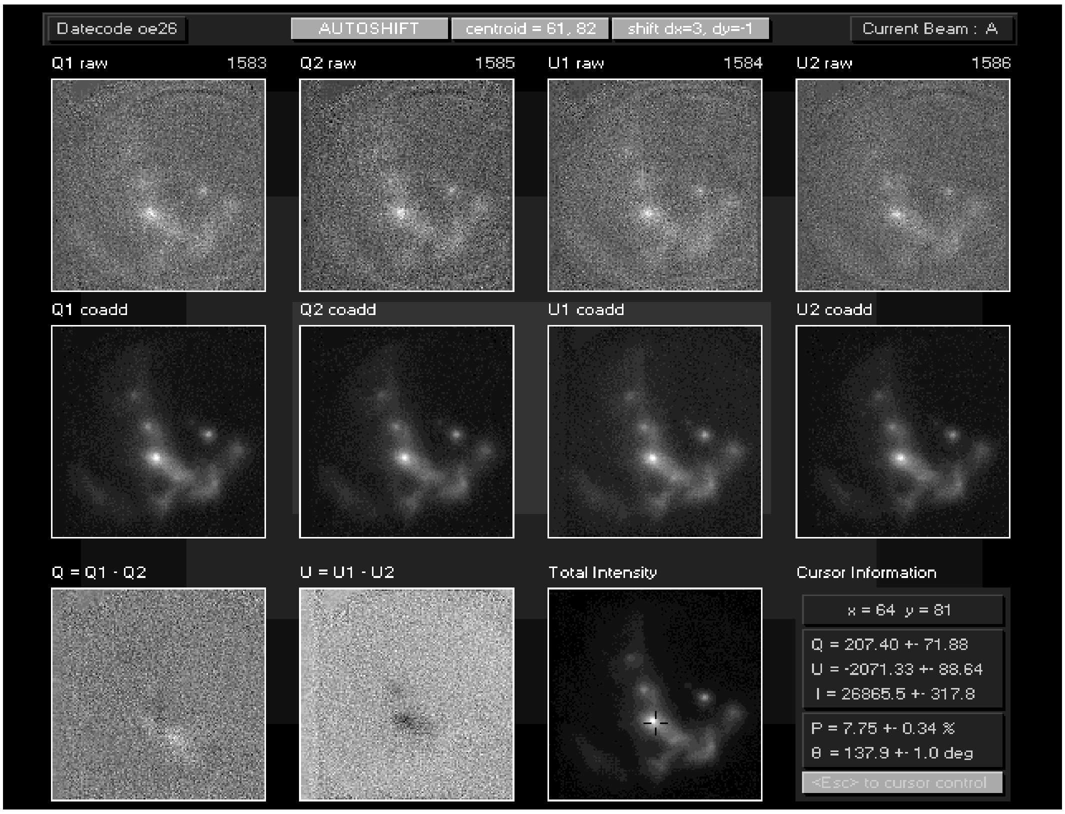

Figure 4: Image of the real time polarimetry reduction screen, showing a field from Sgr A (Galactic Centre).

at each position angle θ. The waveplate is not achromatic and a wavelength dependent correction is applied to the polarization determined. This correction is least at 10 μm and increases to shorter and longer wavelengths. The wiregrid analyser is cold and mounted on the CVF wheel. The Stokes linear polarization parameters (Q, U) are calculated from differences in orthogonal polarization planes:

$Q = I_0 - I_{90} = Q1 - Q2$

$U = I_{45} - I_{135} = U1 - U2$

$I = (I_0 + I_{45} + I_{90} + I_{135})/2 = (Q1 + Q2 + U1 + U2)/2$

The quantities Q1+Q2 and U1+U2 are independent measures of the intensity, and provide a valuable check on data consistency. The circular polarization V is generally negligible.

Figure 4 presents the real-time polarimetry reduction screen showing a field from Sgr A. The top row of images shows the latest integration in each of the waveplate positions, designated Q1, Q2, U1, U2. Each of these images represents about 1 second of integration. Each of these images is coadded separately, allowing for beamswitching and shift-and-add of images if required. The middle row of images shows the running coadd of Q1, Q2, U1, U2. Each of these images is still an intensity image at one of the waveplate positions. The bottom row of images show the current status of the images in the Stokes parameters Q=Q1-Q2, U=U1-U2, and I = (Q1+Q2+U1+U2)/2, and is the total intensity image. Seeing these images allows one to appreciate the need for high signal-to-noise images, as the Q and U Stokes images are differences of intensity images. The panel in the bottom right corner provides numerical readout from the region around the crosshair in the intensity image. Final images of polarized intensity $P = \sqrt{Q^2 + U^2}/I$ and position angle $\theta = \arctan(U/Q)$ are calculated and displayed at the completion of the observing sequence. Should it be necessary to re-reduce the data at a later stage all of the instantaneous Q1,Q2,U1,U2 images are saved to disk. As there are no suitable packages available for dealing with reduction of polarimetric images we have developed a full suite of reduction programs to cope with this most demanding reduction process.

One of the limiting factors in making polarization measurements by this sequential method is that the four intensity values are measured sequentially. This means that small temporal fluctuations, (*e.g.* seeing, weather and tracking errors) become significant when differences are taken. To avoid this problem, we would like to image the orthogonal polarization planes simultaneously. This would be best done with the infrared counterpart of a Wollaston prism, and we are currently investigating such a device, but unfortunately there seem to be few sufficiently birefringent materials at mid-infrared wavelengths, and there are also difficulties optically mating the two prisms of a Wollaston prism.

The signal to noise ratio required to obtain a polarimetric image depends on the degree of polarization in the source, and the precision required. At mid-infrared wavelengths polarizations are generally low, the maximum ever observed is in BN at 12 %, and polarizations of only 2% are common. To obtain a polarimetric image to 1% polarization means that we need a signal to noise ratio (SNR) of 140 in each of the four images Q1, Q2, U1, U2, so that the Q and U difference images end up with a SNR = 100. This results in a intensity image with a minimum SNR of 280 in the faintest region that polarimetric information is required. We also often measure the polarization to less than 1% resulting in extremely high quality intensity images. The instrumental polarization is measured to be $< 1\%$. Under "normal" operating conditions the polarimetric accuracy achieved is limited only by the signal to noise from the source, though systematic effects dominate in marginal operating conditions, limiting the minimum detectable polarization to a few percent.

Calibration of the position angle is effected by two means. An external wire grid polarizer can be placed in the beam to artificially polarize a beam at a known angle and the position angle calibration made from this. Once this "laboratory calibration" is made to determine the true polarization position angle in a few "standard sources" it is possible and more convenient in an observing environment to obtain position angle calibrations from these astronomical sources. The favoured position angle standard is the BN object in Orion because it is bright and highly polarized, making for quick calibration. The position angle calibration is considered good to about 1°.

5 Observational Results

To illustrate the capabilities of the instrument we have included some observing highlights from the instruments first few years of operation. These data were obtained at the Anglo-Australian 3.9-m Telescope (AAT) and United Kingdom Infrared 3.9-m Telescope (UKIRT).

As an example of the instrument's capabilities, figures 5 - 8 show diffraction limited (PSF FWHM = 0.7 arcseconds) 10 μm images of η Carina (Fig. 5), the Galactic Centre (Fig. 6), NGC 1068, a Seyfert galaxy (Fig. 7), and a bipolar proto-planetary nebula Mz-3 (Fig. 8). Superimposed on three of the images are polarization vectors, which indicate the direction of the local magnetic field, while the length of the vector indicates the polarization magnitude.

Polarization at these wavelengths is most often due to emission or absorption from aligned dust grains. In the Galactic Centre the grains are aligned by the ambient magnetic field, presumably by a modified Davis-Greenstein mechanism, and the emitted direction of polarization is at right angles to the field: here the displayed vectors have been drawn orthogonal to the polarization and hence give the field direction. These results confirm and extend earlier work at UKIRT (Aitken et al., 1991) using the GSFC camera with a smaller array, but here the area coverage is greatly

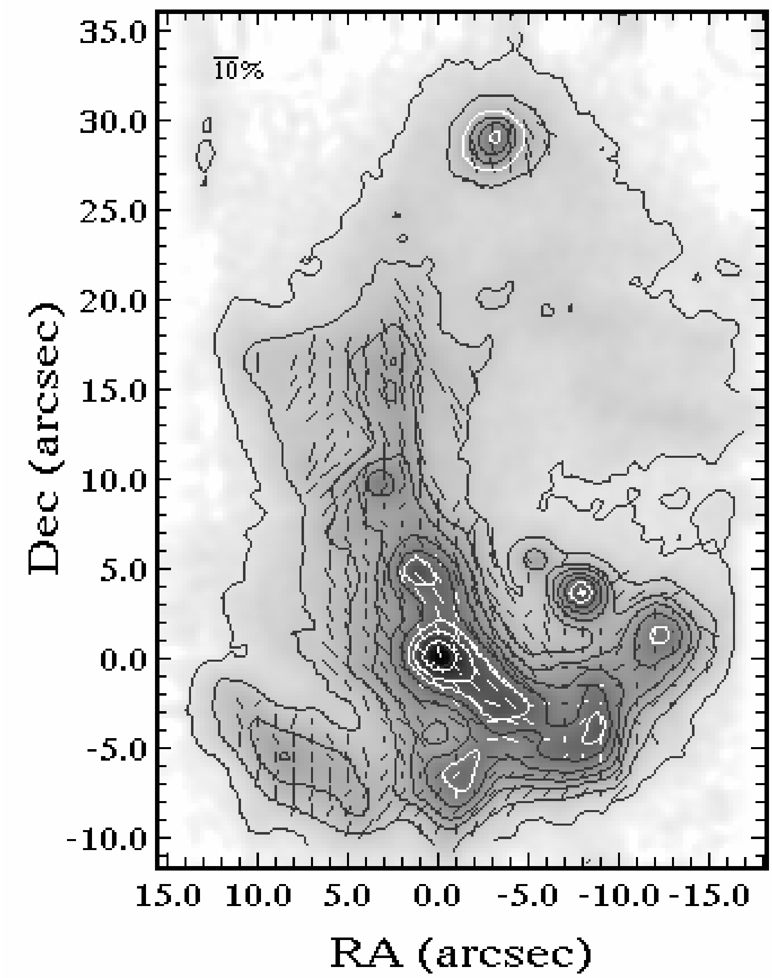

Figure 5: A diffraction limited image of the Galactic Centre at 12.5 μm. The vectors indicate the direction of the magnetic field, and the magnitude of the polarization.

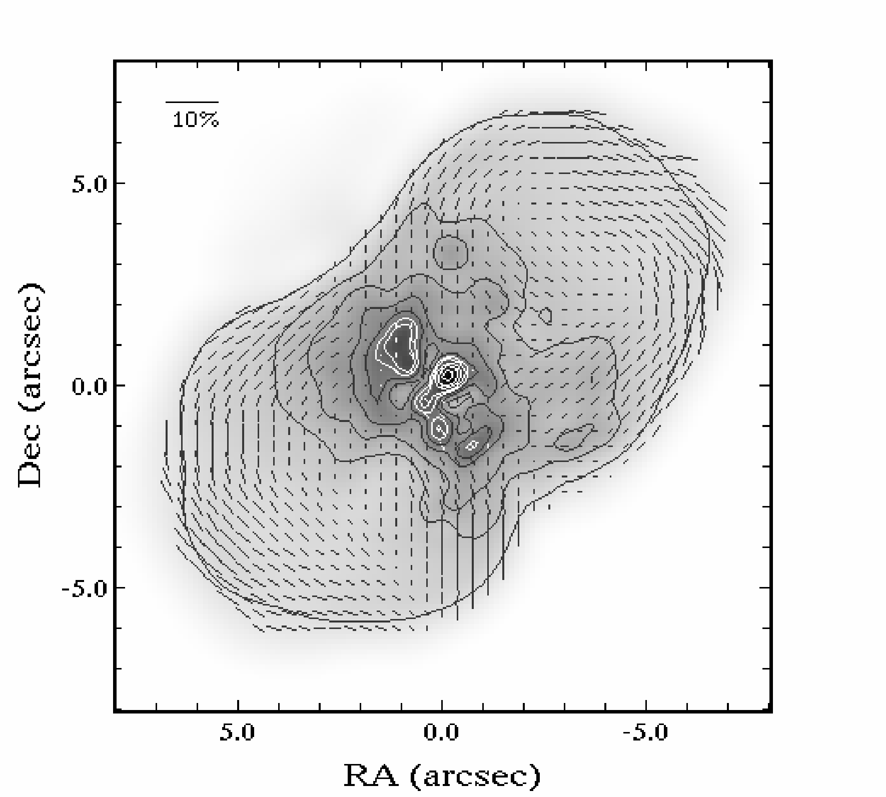

Figure 6: η Carina at 12.5 μm. Image reconstruction (using the pixon-based method) has been employed to produce an effective image resolution of around 0.3 arcseconds, revealing interesting loops near the homonculus core. In this source grain alignment maybe enhanced by streaming, but the polarization vectors still indicate the direction of the local magnetic field.

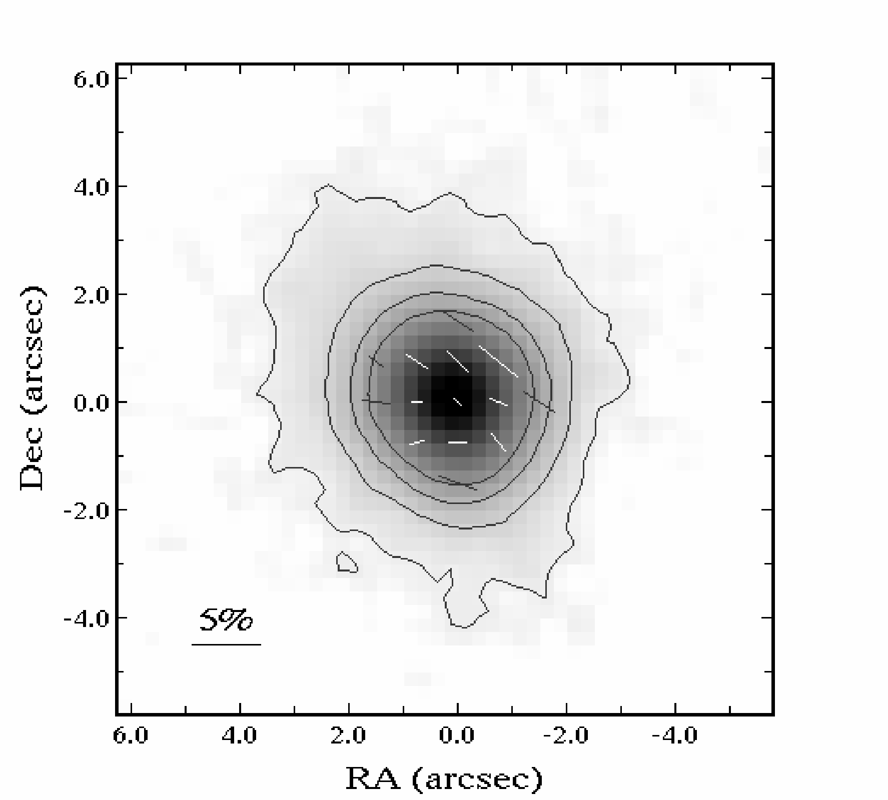

Figure 7: Broad band 10 μm polarimetric image of the Seyfert galaxy NGC 1068. This is the only mid-infrared polarimetric image of a galaxy ever obtained. It shows polarized emission from obscuring dust (magnetic field direction normal to this), plus dilution of the polarization near the galaxy core, probably caused by emission from the active nucleus.

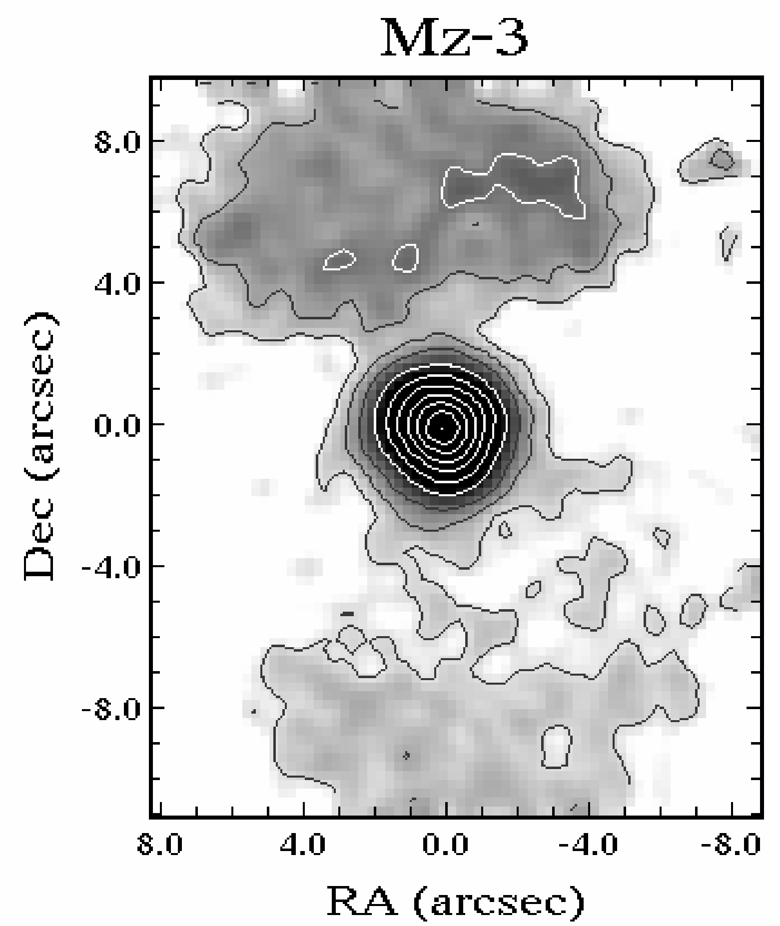

Figure 8: Mz-3 at broad band 10 μm. Here we see bright bi-polar lobes which are radiatively heated by the central source.

increased (from a 15 $\times$ 15 arcsecond region to a 30 $\times$ 45 arcsecond region) in roughly the same observing time. Details of these observations are presented in Aitken, Smith, Moore & Roche (1996).

Due to the extremely high signal-to-noise ratio obtained for the polarimetric image of η Carina we have been able to employ pixon-based image reconstruction to produce an effective image resolution of around 0.3 arcseconds. The reconstructed image shows interesting loops near the core of the source. The magnetic field structure seen here may be the compressed, pre-existing field about η Carina at the time of the 1843 eruption, or the diluted remnant of the stellar field, but it seems more likely that it results from a toroidally magnetized accretion disk in which we suggest the explosion of 1843 occurred. This case is argued in detail in Aitken et al. (1995), and Smith et al., (1995).

The image of NGC 1068 is the only mid-infrared polarimetric image of a galaxy ever obtained. The image data are very similar to that of Braatz et al. (1993) and Cameron et al. (1993). It shows polarized emission from obscuring dust, plus dilution of the polarization near the galaxy core, probably caused by emission from the active nucleus. Details of these observations will be presented in Lumsden et al. (1996).

In Mz-3 we see bright bi-polar lobes which are radiatively heated by the central source. These observations are presented in Quinn et al. (1996).

6 Conclusion

We have successfully built, commissioned and used for science the new imaging polarimeter, NIMPOL. This instrument has been designed to optimize imaging polarimetry at mid-infrared wavelengths, although it functions perfectly well as a straight imaging system too. This instrument is available for collaborative observing programs at the AAT and UKIRT in Hawaii. From the number of requests to use this instrument so far there was an evident need or desire for access to a mid-infrared imaging system in the Southern Hemisphere. We would also like to point out that while the Siding Spring Observatory may not be the ideal location for an infrared observatory, the superb image quality and reliable pointing/tracking of the AAT count for much, and many valuable Southern Hemisphere programs can be accomplished at this telescope with the NIMPOL mid-infrared imaging polarimeter. Anyone interested in using NIMPOL for a collaborative project should contact one of the authors.

Acknowledgements

We would like to acknowledge all those who have worked on this project, but particularly Mr. Marcos de Almeida, Mr. Tony Peebles and Mr. Bill Perrin. Assistance from the observatory staff at the AAT and UKIRT is greatly appreciated, and special thanks to Steve Lee for his cheerful assistance and tolerance during commissioning. This instrumentation program is funded by a grant from the Australian Research Council (ARC), and also from the School of Physics, University College. CHS was funded throughout this work by an ARC Research Fellowship. Thanks also to the Australian Time Allocation Committee (ATAC) and SERC PATT for the award of observing time on the AAT and UKIRT.

References

Aitken D.K., Smith C.H., Roche P.F., 1989, *MNRAS,* **236,** 919

Aitken D.K., Smith C.H., Roche P.F., Wright C.M., 1990, *MNRAS,* **247,** 466

Aitken D.K., Gezari D.Y., Smith C.H., McCaughrean M., Roche P.F., 1991, *Ap. J.,* **380,** 419

Aitken D.K., Wright C.M., Smith C.H., Roche, P.F., 1993, *MNRAS,* **262,** 456

Aitken D.K., Smith C.H., Moore T.J.T., Roche P.F., 1995, *MNRAS,* 273, 359

Aitken D.K., Smith C.H., Moore T.J.T., Roche P.F., 1996, ESO Workshop on The Galactic Centre in Conf Series ASP.

Braatz J.A., Wilson A.S., Gezari D.Y., Varosi F., Beichman C.A., 1993, *Ap.J.,* 409, L5

Cameron M., Storey J.W.V., Rotaciuc V., Genzel R., Siebenmorgen R., Lee T.J., 1993, *Ap.J.,* 419, 136

Gonatas D.P., Engargiola G.A., Hildebrand R.H., Platt S.R., Wu X.D., Davidson J.A., Novak G., Aitken D.K., Smith, C.H., 1990, *Ap. J.,* **357,** 132

Lumsden S., Moore T.J.T, Smith C.H., Bland-Hawthorn J., Fujiyoshi T., 1996, *MNRAS,* (in preparation)

Quinn D.E., Fujiyoshi T., Moore T.J.T., Smith C.H., Smith R.G., 1996, *MNRAS,* (in press)

Smith C.H., Aitken D.K., Roche P.F., 1990, *MNRAS,* **246,** 1

Smith C.H., Aitken D.K., Moore T.J.T. Roche P.F., Puetter R.C, Pina, R.K., 1995, *MNRAS,* 273, 354